Ionic conductivity of chemically lithiated $YBa_2Cu_3O_7$: NMR and impedance spectroscopic studies

Ionic conductivity of chemically lithiated $YBa_2Cu_3O_7$: NMR and impedance spectroscopic studies

A Várez†, C León‡, J Santamaría‡, J M Rojo§, J Sanz§, E Morán‖, F Sánchez-Quesada¶ and M A Alario-Franco‖

† Departamento de Ingeniería, Escuela Politécnica Superior, Universidad Carlos III de Madrid, 28911 Leganés, Spain
‡ Departamento de Física Aplicada III, Facultad de Ciencias Físicas, Universidad Complutense, 28040 Madrid, Spain
§ Instituto de Materiales, CSIC, C/Serrano 115, 28006 Madrid, Spain
‖ Departamento de Química Inorgánica, Facultad de Ciencias Químicas, Universidad Complutense 28040 Madrid, Spain
¶ Departamento de Física Aplicada III, Facultad de Física, Universidad Complutense, 28040 Madrid, Spain

Abstract. High-T_c superconducting $YBa_2Cu_3O_7$ ceramic samples are lithiated by the reaction with n-butyllithium. For lithium nominal contents less than unity per formula the presence of '123' and '124' phases are deduced from x-ray diffraction and high-resolution electron microscopy experiments. NMR and impedance spectroscopy techniques have been conducted in a sample with a nominal Li content of 0.9 per formula. Spin–lattice relaxation times and electrical conductivity relaxation (ECR) are measured as a function of temperature. NMR and ECR data are interpreted in terms of a stretched exponential decay function in the time domain. Microscopic activation energies for lithium motion of 0.49 eV (NMR measurements) and of 0.41 eV (ECR) are deduced for short range motion. Activation energies for long range motion of 0.98 eV (NMR) and 1.03 eV (ECR) are also deduced.

1. Introduction

Insertion reactions have been widely used to modify the transport properties of solids. In this kind of reaction, starting materials have to meet some requirements such as having tunnels with empty available sites and reducible metallic cations [1, 2]. Perovskite-related structures have been extensively employed to perform insertion reactions [3]; in particular, the high-T_c superconducting $YBa_2Cu_3O_7$ has a relatively open structure and Cu ions which can change their oxidation state. Inserting small monovalent ions in the high-T_c superconductors (HTSCs) may be of interest since it offers a way to change the hole carrier concentration by the transfer of electrons from the inserted atoms into the hole band. In this field it is worth referring to the pioneer work of Reilly *et al* [4], in which the insertion of hydrogen in $YBa_2Cu_3O_7$ is discussed. In previous papers [5–8] we have reported on the reaction of n-butyllithium with $YBa_2Cu_3O_7$ to produce a new series of 'composite' materials, $Li_xYBa_2Cu_3O_7$ ($0 < x \leqslant 2.1$), which become ionic conductors while retaining their superconducting properties up to a limited amount of inserted lithium. The volume fraction of the superconducting phase depends on the degree of insertion, diminishing with the increase in the lithium content, and superconductivity disappears for values of x higher than 1.5 [7]. The process is not at all simple and has important consequences at the

microstructure level: extended defects or disordered intergrowths are produced which, as shown by high-resolution electron microscopy (HREM), have different compositions and structures: the so-called '124' ($YBa_2Cu_4O_8$) and/or '247' ($Y_2Ba_4Cu_7O_{15}$) phases appear [8]. It is worth recalling that the '124' structure was formerly observed as a planar defect in '123' partially decomposed samples [9] and also detected in multiphased '123' thin films [10]. This lithiation process cannot properly be considered a topotactic reaction but it constitutes a new procedure for the preparation of new cuprates which are closely related to the HTSC materials [11]. Besides, the coexistence of ionic conductivity and superconductivity in the same sample is an interesting issue from the point of view of potential applications as cathodic materials.

The aim of this work is to study, by using both NMR and impedance spectroscopy, the lithium ionic mobility in these kinds of materials. The combined use of NMR and admittance spectroscopy is a conclusive way to establish ion mobility and can help shed light on the dynamics of the conduction process. Significant departures from the classical Debye (electrical conductivity relaxation) and BPP (nuclear spin relaxation) models occur in many ion conducting systems: a power law dependance of the a.c. conductivity on frequency, strongly non-Debye modulus peaks and asymmetric $1/T_1$ against $1/T$ plots have been frequently observed [12]. Those departures, arising from ion–ion correlations, have been empirically interpreted in terms of stretched exponential decays ($\exp(-t/\tau)^\beta$) in the time domain, β being a measure of the correlation strength and τ a thermally activated correlation time for ion motion ($\tau = \tau_0 \exp(E/kT)$). One aspect which is still a subject of controversy is whether the β and E values deduced from both techniques should be the same or not [13, 14]. Recently, Ngai has suggested [13] that the parameters characterizing the dynamics of the ionic system, β and E, can be used to obtain a microscopic activation energy, E_a. In this way, the values of β and E deduced from both techniques have to result in the same microscopic activation energy E_a, obtained as the product βE. The NMR and complex admittance measurements on lithiated $YBa_2Cu_3O_7$ samples have thus been analysed in terms of stretched exponential decay functions and the microscopic activation energy for Li^+ motion has been deduced.

2. Experimental details

Materials were obtained by the room-temperature reaction of $YBa_2Cu_3O_7$ samples with solutions of n-butyllithium in the appropriate conditions [5]. The approximate formal Li/'123' molar ratio was established by readily extracting lithium from the samples using an iodine solution in acetonitrile and taking into account the amount of $YBa_2Cu_3O_7$ sample used; lithium iodide is formed and the remanent iodine is backtitrated with a standard thiosulphate solution.

Powder x-ray diffraction (XRD) experiments were performed on a Siemens D-5000 set-up with monochromatic Cu $K\alpha$ radiation, using silicon as internal standard. HREM and electron diffraction (ED) were performed on a Jeol 4000 EX instrument operated at 400 kV. Specimens for transmission electron microscopy were prepared by grinding, dispersing in n-hexane and putting a few droplets on a carbon-coated copper grid; they were only exposed to the atmosphere while mounting the grid in the sample holder.

^7Li NMR spectra were recorded with an SxP 4/100 Bruker spectrometer equipped with an FT unit. The frequency used was 34.95 MHz corresponding to an external magnetic field of 2.11 T. The number of accumulations was 200 in order to get a signal to noise ratio higher than 20. A $\pi/2$ pulse of 3 μs and a period of 5 s between successive accumulations

were chosen to optimize the signal intensity in RT experiments. Determination of spin lattice relaxation times, T_1, was carried out in the temperature range 213–523 K by using a $\pi/2$–$\pi/2$ sequence.

Complex admittance was measured in the frequency range 10 Hz–10 MHz and at temperatures ranging between 300 and 600 K using an automatically controlled HP4192A impedance analyser. The samples consisted of cylindrical pellets 5 mm in diameter and 0.7 mm thick. Electrodes were Au spots deposited by evaporation. Temperature was limited to 600 K to avoid deoxygenation of the samples. Measurements were conducted under an N$_2$ flow.

3. Results and discussion

3.1. Structural characterization

As already shown [7] the amount of inserted lithium, x, increases with the reaction time: stirring 1 g of YBa$_2$Cu$_3$O$_7$ with 1.6 M n-butyllithium solution for 24 hours produces a sample with a nominal lithium content per formula of $x = 0.13$ while 1000 hours of stirring in the same conditions leads to contents of $x = 2.1$; below $x = 1.5$ lithiated samples still look black while above that limit they appear greenish. In this work, the lithium content of the studied sample was $x = 0.9$.

XRD patterns of the lithiated samples are very close to those of the fresh material, and all the reflections of the orthorhombic '123' phase appear. Extra peaks corresponding to the '124' phase are also observed whose intensity increases with Li content. Reflections of the so-called 'green phase' Y$_2$BaCuO$_5$ are observed for high Li contents, this explaining the greenish appearance of the samples for $x > 1.5$. An increment of the background in the patterns is also detected in these samples, characteristic of the loss of crystallinity in this type of reaction [15]. Nevertheless, the '123' phase remains orthorhombic and its cell parameters do not change appreciably (table 1). When the lithium is removed from the lithiated samples by means of an iodine solution, the XRD patterns still show the extra peaks; this is one of the strongest indications that this process is not reversible. A recent electrochemical study on the reduction of YBa$_2$Cu$_3$O$_7$ with lithium has confirmed the non-reversibility of the reaction [15, 16]. This finding is reasonable if we take into account that the formation of the '124' from the '123' phase involves a substantial atomic reorganization. The lower Cu content of Y$_2$BaCuO$_5$ phase probably compensates the additional CuO plane of the '124' phase. Of course we cannot exclude the presence of small amounts of green phase (non-detectable by XRD) in the samples with low Li contents.

Table 1. Unit cell parameters corresponding to the lithiated materials.

Li/Y	a (Å)	b (Å)	c (Å)	V (Å^3)
0.17	3.8231(2)	3.8842(2)	11.678(6)	173.4(1)
0.27	3.8235(6)	3.8851(6)	11.674(6)	173.4(1)
0.44	3.8239(2)	3.880(5)	11.684(2)	173.3(3)
0.57	3.8233(9)	3.8819(2)	11.686(4)	173.4(1)
1.2	3.8251(6)	3.8882(2)	11.601(3)	172.5(1)
2.1	3.8170(9)	3.881(1)	11.688(4)	173.1(2)
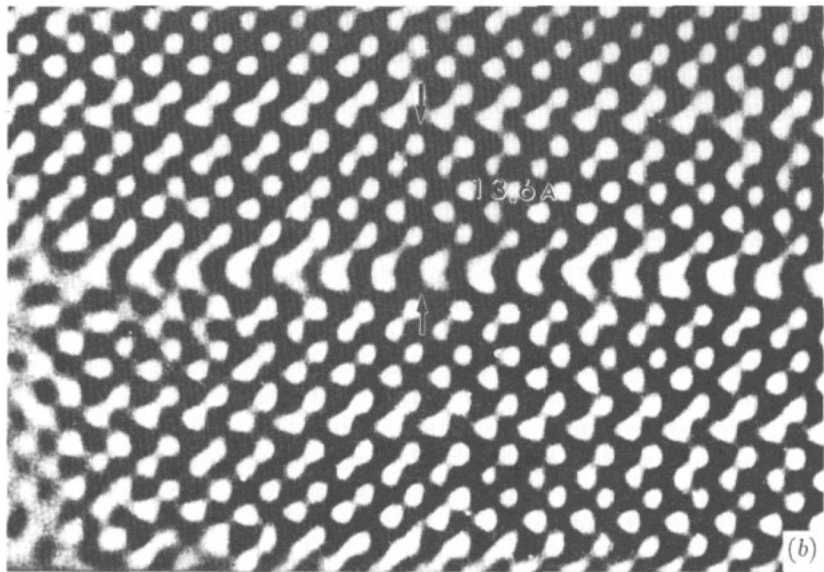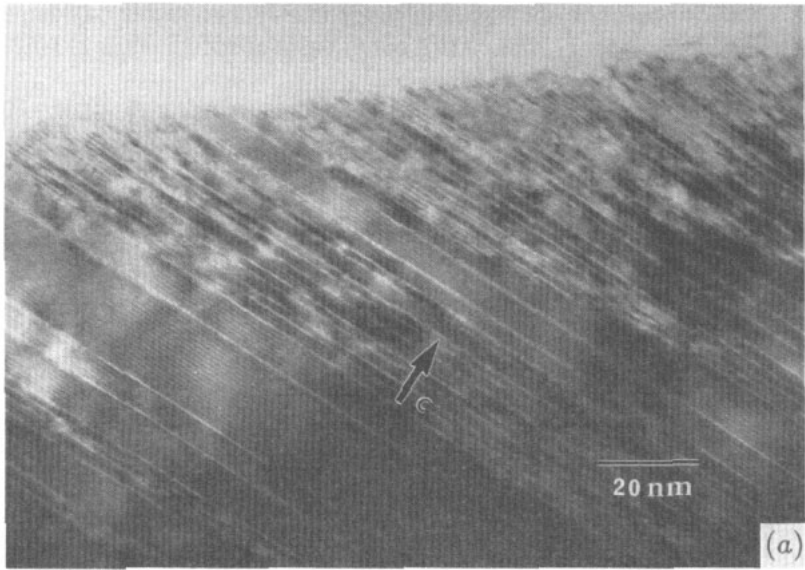
Figure 1. (a) Transmission electron micrograph of the $Li_{0.9}YBa_2Cu_3O_7$ sample taken along the [0 1 0] or [1 0 0] zone axis. Extended defects can be observed along the c^* axis of the '123' matrix leaded by means of the lithiation process. (b) Magnification of a defect zone of (a), where the interplanar distance of 13.6 Å can be clearly seen [24]. This distance corresponds to half the unit cell of '124' phase.

Transmission electron micrographs corresponding to samples with low lithium content ($x < 1$) show disordered extended defects, running perpendicularly to the c-axis (figure 1(a)). These become more frequent when the x value is increased. Electron diffraction patterns corresponding to those images show a marked streaking in all rows parallel to the c^* axis while no extra spots or streaks are observed in other regions of the

reciprocal cell; in particular the basal plane *ab* is not affected upon lithiation. At higher magnifications (figure 1(*b*)), the basic Ba–Y–Ba perovskite blocks characteristic of the '123' structure are separated by double $[CuO_4]$ chain layers along the *c* axis in the defect area. A new interplanar distance along that direction can be measured, $d = 13.6$ Å, corresponding to half of the *c* parameter of the '124' structure, together with the $d_{001} = 11.8$ Å distance characteristic of the '123' phase. HREM micrographs and the corresponding simulated images let us confirm this point. This kind of defect can in fact be considered as intergrowths of different polytypoids of the $Y_2Ba_4Cu_{6+n}O_{14+n}$ family of phases [11]. The microstructure of materials with high lithium contents ($x > 1.2$) are markedly different: their ED patterns and the corresponding images have to be interpreted on the basis of the '124' structure (lattice parameters, $a = 3.842$ Å, $b = 3.871$ Å, $c = 27.24$ Å, S G *Ammm*) [17] and strain, disorder, and even corrugated planes are frequently observed.

3.2. NMR data

The ^7Li NMR spectra ($I = \frac{3}{2}$), recorded at increasing temperatures (figure 2(*a*)), show only one line centred at the Li resonance frequency that progressively narrows as temperature increases. The variation of the full width at half maximum (δ) with $1000/T$ is plotted in figure 2(*b*). At temperatures below 293 K the linewidth is almost constant indicating that interactions of Li with the environment are constant and Li remains at times $\tau > (\Delta\omega)^{-1}$ (NMR linewidth inverse) in fixed structural positions. At temperatures higher than 345 K the linewidth decreases as a consequence of the motion of Li ions, which induces a progressive cancellation of the interactions of the Li with the environment. This phenomenon happens when the correlation time of Li motion, τ_s, is smaller than $(\Delta\omega)^{-1}$ (motional narrowing effect). Above 473 K a slight increase in $1/T_2$ is detected which cannot be explained on the basis of structure modifications. XRD experiments performed in this temperature range did not show structural changes. Since the slight increase in $1/T_2$ takes place at the edge of our measuring domain, we cannot further increase the temperature to address this point.

The spin–lattice relaxation rate ($1/T_1$) against temperature inverse ($1000/T$) is plotted in figure 2(*c*). At temperatures below 320 K a *quasiplateau* is again observed. Above this temperature $1/T_1$ increases and attains a maximum at 493 K. Detection of a *plateau* at low temperatures should be related to the paramagnetic interaction between magnetic moments of Li nuclei and non-coupled electrons. Subtraction of the constant paramagnetic contribution, $(1/T_1)_p$, from the experimental values $(1/T_1)_{obs}$, gives the corrected values, $1/T_1 = (1/T_1)_{obs} - (1/T_1)_p$, from which lithium mobility can be analysed. The spin relaxation rate is related to the spectral density function, $J(\omega_L)$, according to the following expression:

$$1/T_1 = A\{J(\omega_L) + 4J(2\omega_L)\} \tag{1}$$

where ω_L is the Larmor frequency and A is the coupling constant. Assuming a stretched exponential decay $\exp(-t/\tau_s)^{\beta_s}$ for the correlation function, the spectral density $J(\omega_L)$ can be expressed as

$$J(\omega_L) = \int_0^\infty e^{(-t/\tau_s)^{\beta_s}} e^{-i\omega_L t}\,dt \tag{2}$$

where the correlation time τ_s can be written as $\tau_{s0}\exp(E_s/kT)$ and E_s plays the role of an activation energy for extended ion motion. This energy is related to the single-ion microscopic activation energy, E_a, through $E_s = E_a/\beta_s$. Activation energies for long- (E_s)
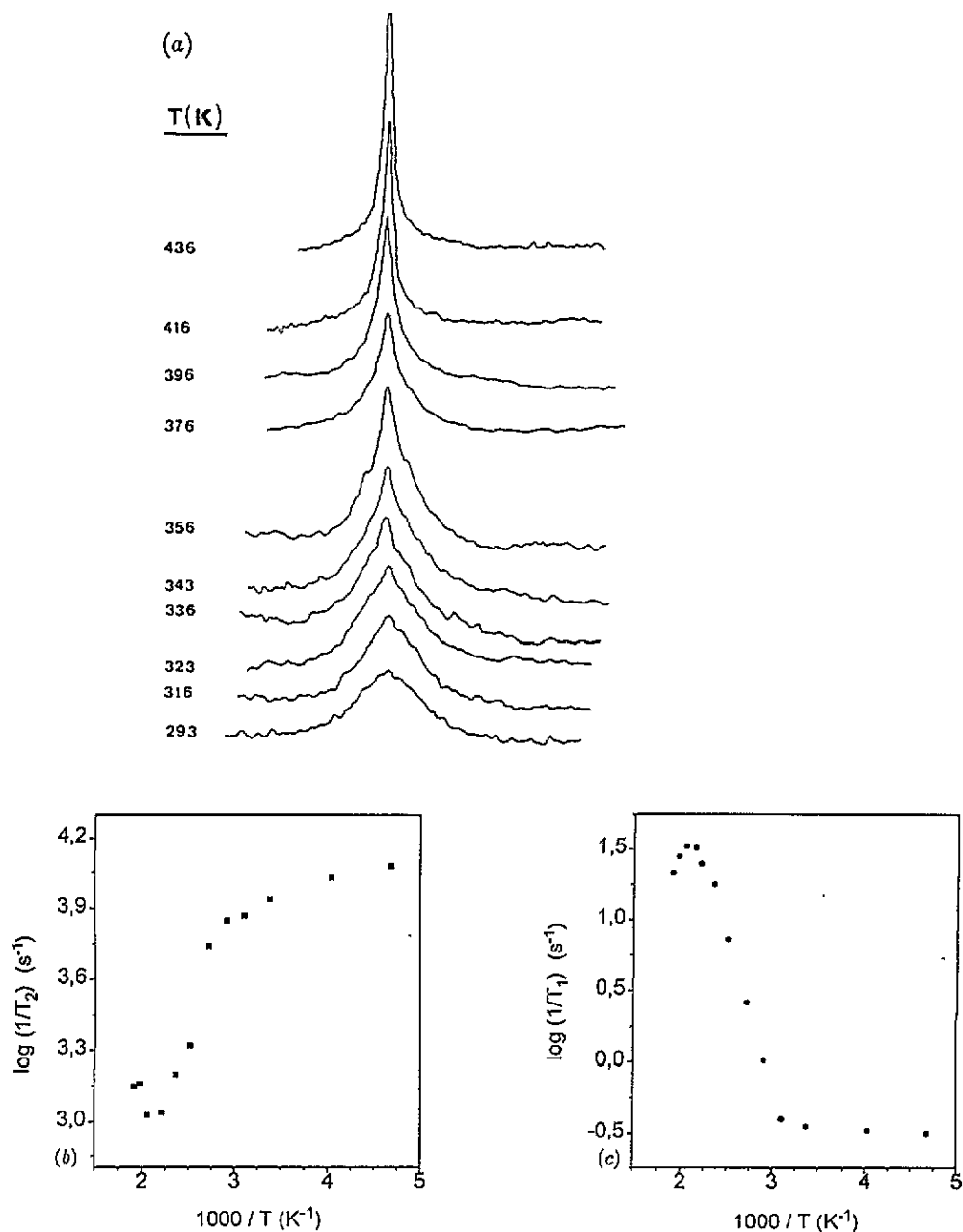
Figure 2. (a) ^{7}Li NMR spectra (34.95 MHz) recorded at different temperatures on the Li$_{0.9}$YBa$_2$Cu$_3$O$_7$ sample. Temperature dependence of (b) T_2^{-1} and (c) T_1^{-1} for the same sample.

and short- (E_a) range motions can be obtained from the slope of the linear portions of the log $(1/T_1)$ against $1000/T$ curve at both sides of the maximum. On the low-temperature side an activation energy $E_a = 0.49$ eV has been deduced. From the maximum, a correlation time of 2.77×10^{-9} s at 493 K has been obtained. The lack of data in the high-temperature region prevents the accurate determination of the corresponding activation energy and the value of

β_s. Nevertheless, the best fit of the $1/T_1$ was obtained for $\beta_s = 0.5$ and $E_s = 0.98$ eV.

3.3. Complex admittance measurements

Complex susceptibility has been obtained from admittance measurements in the usual way. We have chosen a mixed permittivity–conductivity representation to present dielectric data. The real part of the permittivity and the real part of the conductivity are plotted in figures 3(a) and 3(b) respectively, at several temperatures. The conductivity ($\sigma^* = i\omega\epsilon^*$) representation is frequently used in charge-carrier-dominated systems, while permittivity (ϵ^*) is preferred for the description of dielectric phenomena. Some features in the real part of the permittivity, like the power law dependence at low frequencies observed in figure 3(a), are obscured in the conductivity representation. However, σ (calculated as $\epsilon''\omega$) plots underline power law departures from the pure non-dispersive d.c. conductivity at high frequencies. This behaviour is characteristic of correlation mechanisms among charge carriers.

The real part of the permittivity, from which a constant high-frequency value has been subtracted ($\epsilon' - \epsilon_\infty$), as shown in figure 3(a), shows a steep power law increase towards low frequencies for temperatures higher than 420 K in the available frequency range. This behaviour is known as anomalous low-frequency dispersion (ALFD) and has often been observed in ion conducting solids [18]. Two straight lines have been drawn to fit the low-frequency data to illustrate their almost constant slope over the whole temperature range. At high frequencies a crossover to another power law regime with a smaller slope can be observed, so that the real part of the permittivity can be expressed as

$$\epsilon' - \epsilon_\infty = A(T)\sin(n\pi/2)\omega^{(1-n)} + B(T)\sin((1-p)\pi/2)\omega^{-p} \qquad (3)$$

where the exponents p and n account for the ALFD and for the high-frequency power law regime respectively and where $B(T)$ and $A(T)$ contain the temperature dependence of the permittivity. A fit to this expression is also presented in figure 3(a).

Figure 3(b) displays the frequency behaviour of the real part of the conductivity for several temperatures. It can be observed that, in the low-temperature range, the conductivity is essentially non-dispersive at low frequencies, but that there is a temperature-dependent crossover to a power law regime of the form ω^n with $n = 0.6$ at higher frequencies. Actually, the conductivity contains two parts, a dispersive part related to the permittivity by Kramers–Kronig transforms and a non-dispersive d.c. contribution, so that it can be written as

$$\sigma(\omega) = \sigma_{d.c.} + A(T)\cos(n\pi/2)\omega^n. \qquad (4)$$

The d.c. term practically overshadows the contribution coming from the ALFD except at the higher temperatures, at which a small dispersive effect can be noted. In this case, the conductivity adopts the form

$$\sigma(\omega) = \sigma_{d.c.} + A(T)\cos(n\pi/2)\omega^n + B(T)\cos((1-p)\pi/2)\omega^{1-p}. \qquad (5)$$

The a.c. power law regime of the conductivity has been widely observed in ionic conductors and also in conducting polymers, heavily doped semiconductors and amorphous insulators exhibiting hopping transport. In our case, it seems reasonable that this regime is due to ionic mobility. The non-Debye response of the conductivity, of the form $(i\omega)^n$, is often termed 'universal dielectric response' [18, 19], and corresponds to stretched
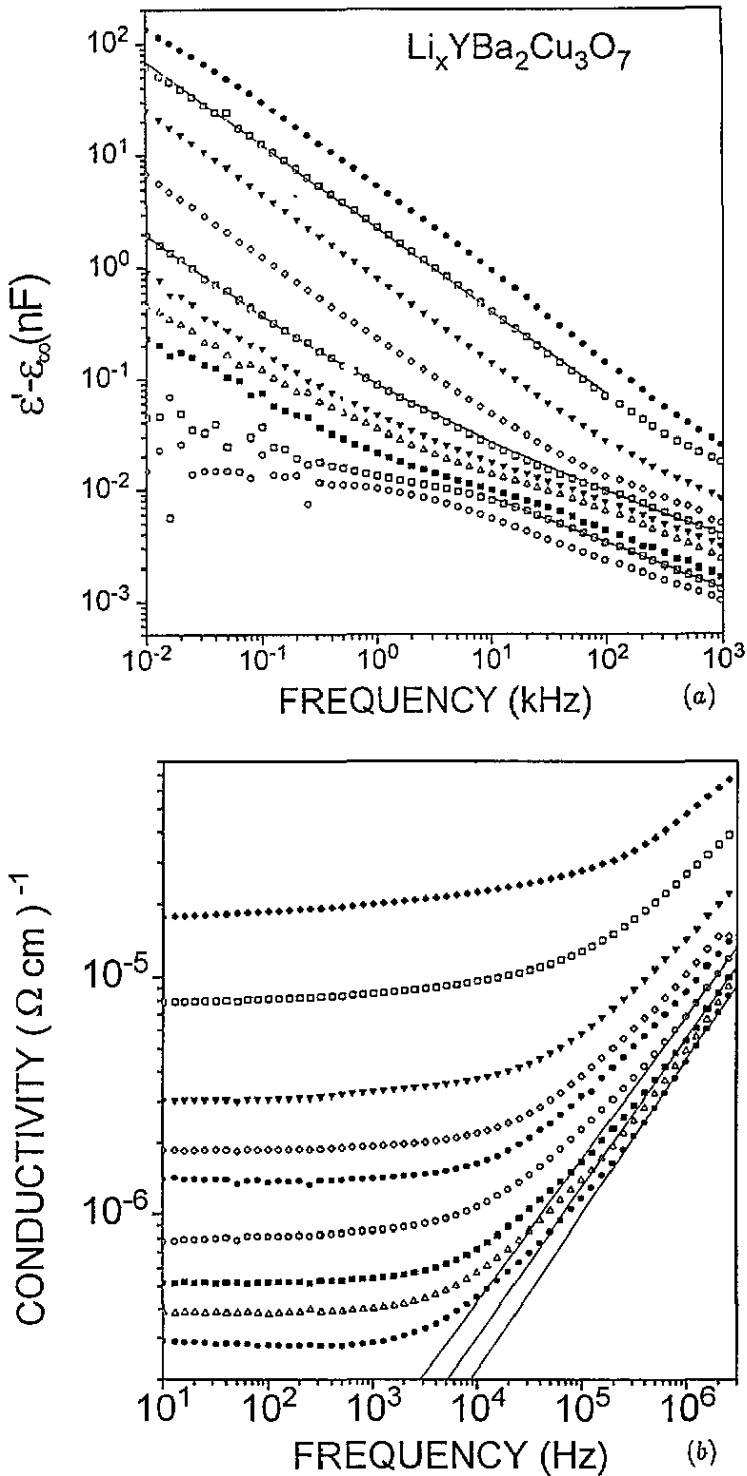
Figure 3. (a) Frequency dependence of $\epsilon' - \epsilon_{\infty}$ at several temperatures (in the range of 333–586 K) for the lithiated sample. Fitting of data at low and high frequencies, plotted as full lines, is introduced to illustrate the two identified regimes. (b) Real part of conductivity against frequency in the temperature range of 333–500 K for the lithiated sample. The fitting of the data at the highest frequency is plotted as full lines, showing a power law dependence ($\sigma \propto \omega^{n}$).

exponential decay functions in the time domain of the Kohlrausch–Williams–Watts (KWW) form [20]:

$$\Phi(t) = \exp(-t/\tau)^\beta \qquad (6)$$

where $\Phi(t)$ is the normalized decay of the electric field E at constant displacement vector D. The departure from the ideal $\beta = 1$ $(n = 0)$ Debye case has been interpreted in terms of correlated ion hopping due to many-body interactions among ions. Frequency and time domain pictures are actually equivalent and $\beta = 1 - n$ holds approximately [21]. Customarily the time response is obtained from the dielectric modulus $M^* = 1/\epsilon^*$: the imaginary part exhibits a peak from which β and τ can be obtained from the following expression:

$$M^*(\omega) = \frac{1}{\epsilon_\infty}\left[1 - \int_0^\infty \frac{d\phi(t)}{dt}e^{-i\omega t}\,dt\right]. \qquad (7)$$
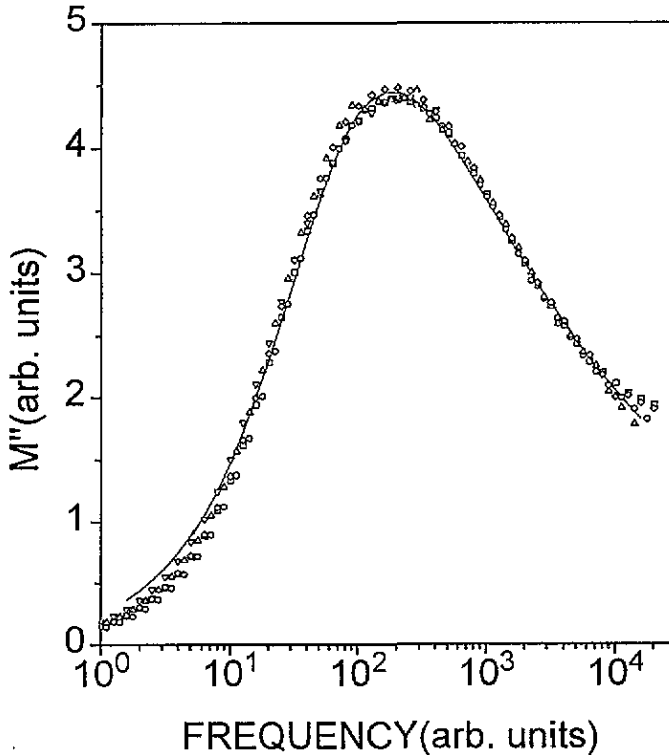

Figure 4. Normalized imaginary part of dielectric modulus against frequency. The shape of the peaks corresponding to different temperatures are similar. A value of $\beta = 0.4$ is obtained after fitting of data to expression (7).

Due to instrumental limitations we only observed this peak at temperatures below 400 K and at frequencies above 5×10^3 Hz, where the conduction was mainly due to ions (power-dependent regime). The fitting of the imaginary modulus to expression (7) yielded β values

of 0.4. Normalized modulus data are presented in figure 4, showing a relatively good fit to $\beta = 0.4$ in frequency range where the conductivity is dominated by ion motion. Modulus peaks normalized to a single curve point to a single relaxation process with a single activation energy. The stretching of the decay function accounts for correlations among moving ions and not for a true distribution of relaxation times. The value obtained for β agrees with the $1 - n$ exponent obtained from conductivity measurements in the same temperature range. Nevertheless, since the temperature range in which we observed the modulus peak was relatively narrow and even in this temperature range the results could be influenced by the electronic conductivity, we have based our discussion on the conductivity formalism.
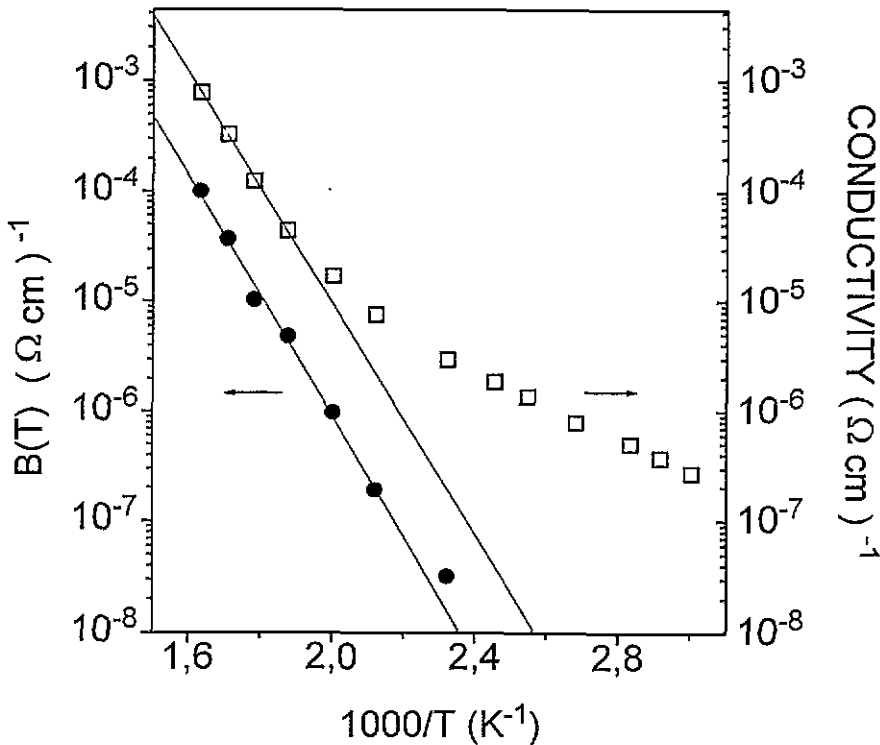

Figure 5. Temperature dependence of d.c. conductivity (□) and term $B(T)$ (●) in an Arrhenius plot.

It is worthwhile commenting that no effects of blocking at grains or electrodes have been observed in permittivity or conductivity plots, probably as a result of a limited frequency and temperature range, although, as quoted below, the ALFD might be an indication of it. The blocking of charge carriers causes steep decreases (with slope higher than unity) in the conductivity towards zero (electrodes) or towards a finite value (partially blocking grain boundaries) and plateaus in the real part of the permittivity. None of these effects have been observed in figures 3(a) and (b), indicating that higher temperatures and/or lower frequencies are required to observe these effects: frequencies are limited by our experimental system and higher temperatures would cause changes in oxygen content or activate oxygen mobility.

A non-linear least-squares fitting routine has been used to obtain the parameters $A(T)$, $B(T)$, $\sigma_{d.c.}$, p and n from complex admittance data (expression (5)). The temperature dependences of $\sigma_{d.c.}$ and $B(T)$ have been plotted in figure 5 in an Arrhenius fashion yielding two linear regimes for the d.c. conductivity with activation energies of 1.03 and 0.3 eV respectively and an activation energy of 1.01 eV for $B(T)$. The evaluation of the ionic conductivity from complex admittance measurements is complicated by the presence of an electronic conductivity superimposed on the ionic conductivity. Although lithium insertion will change the Cu oxidation state, reducing the free carrier density, the remaining electrons will give rise to the electronic conductivity. In fact, lithium insertion causes a decrease of the superconducting fraction in the sample as proven by magnetic susceptibility measurements [7], but the sample is still superconducting. In this way, the two regimes observed in figure 5 for $\sigma_{d.c.}$ may be interpreted in terms of an electronic conductivity which dominates at low temperatures ($E = 0.3$ eV) and a stronger activated ionic conductivity ($E = 1.01$ eV), in parallel with it, which dominates at high temperatures. This interpretation is supported by the NMR results which show that Li mobility increases rapidly at 400 K.

The strong low-frequency dispersion obtained in the real part of the permittivity has often been reported as due to ion motion, but its origin has not been established unambiguously. For some authors it is associated with blocking phenomena at internal boundaries (grain or phase boundaries) or at electrodes. However, a distribution of barrier heights at grain boundaries or charge build-ups at electrodes could hardly yield the perfect power law displayed in figure 3(a). On the other hand, it has been claimed that the ALFD corresponds to an independent regime in the dispersive ionic conductivity [22]. A discussion on the origin of the ALFD is beyond the scope of this paper; suffice it to say that, in any case, it is closely linked to ion motion in the sample. In this sense, the activation energy deduced from the real part of the permittivity has to be related to the activation energy for ion motion. In fact, the activation energy obtained from $B(T)$, close to 1 eV, is in very good agreement with the one deduced from the high-temperature slope of the d.c. conductivity, suggesting that ALFD contribution is indeed mainly due to ion motion.

A comparison between the results obtained by both techniques, NMR and conductivity relaxation, may offer further support for ascribing the high-temperature slope of the d.c. conductivity to ion motion. The comparison of the activation energies deduced from spin–lattice and conductivity relaxations has recently raised much interest. In particular Ngai [13], following his phenomenological model for treating relaxation in glass systems, has shown that the relation $\beta_\sigma E_\sigma = \beta_s E_s$ holds; where E_σ and E_s are the activation energies of the ionic conductivity and the one obtained from NMR at extended motion respectively, and where β_σ, β_s are the decay parameters deduced from both techniques. The product βE gives a microscopic energy, E_a, for lithium motion. If, on the basis of the preceding reasoning (see table 2), we take for β_σ the value of 0.4, and for E_σ that of 1.03; then the obtained $\beta_\sigma E_\sigma$ value is 0.41 eV, which is in very good agreement with the microscopic energy, E_a, deduced from NMR measurements, 0.49 eV, and might thus be ascribed to a microscopic activation energy for Li^+ motion. On the other hand, if we use the same argument for the other activation energy $E_\sigma = 0.3$ eV, a value of 0.12 eV is obtained, which is very low to be associated with ions.

Table 2. Activation energies and β values deduced from conductivity and NM measurements.

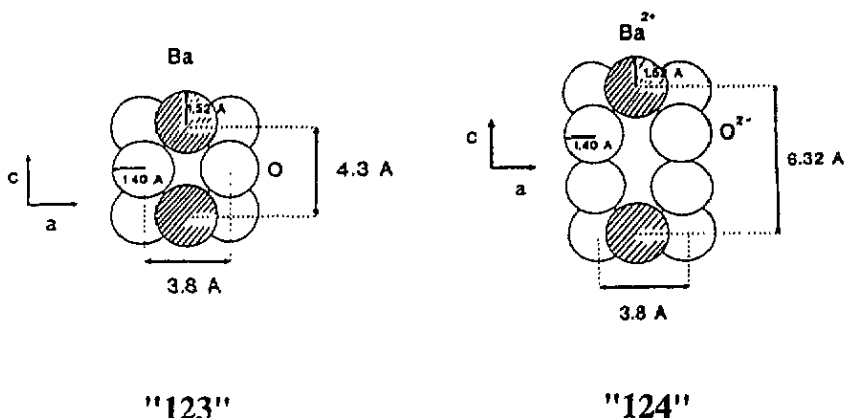|	n	β	E_σ (eV)	βE_σ (eV)
NMR	—	0.5	0.98	0.49
Conductivity	0.6	0.4	1.03	0.41

Figure 6. Schematic drawing of the tunnels corresponding to the '123' and '124' structures, using the Shannon and Prewitt radii on the basis of an ionic rigid-sphere model.

One remaining question is whether Li moves in the 123 phase or is restricted to the 124 phase. Although, as quoted in the structure section, we cannot exclude the presence of small amounts of 'green phase' (non-detectable by XRD), its tightly packed structure makes Li insertion very unlikely; in fact, this compound has not reacted with n-butyllithium. The absence of any systematic change in the 123 cell dimension during Li incorporation (table 1), together with the fact that upon lithiation the material remains superconducting but the superconducting fraction decreases, point to the absence of Li from the 123 phase. Furthermore, from static lattice calculations [23] we have determined the most probable positions for Li ions, both in 123 and in 124 structures. These appear to be the positions located between adjacent Ba ions and in the Y planes, as sketched in figure 6. However, much higher barriers connecting those structural sites have been obtained in the 123 than in the 124 phases. We have to stress that our calculations should be taken only as indicative and, despite their complexity, dynamic calculations would provide a more realistic answer. Nevertheless, the results obtained are those 'expected' for conventional ionic conductors since in the 124 phase a wider space exists between the Ba ions as the result of the introduction of an extra CuO plane (see figure). Moreover, recent electrochemical results indicate that $YBa_2Cu_4O_8$ reversibly inserts lithium in a much higher amount than that corresponding to $YBa_2Cu_3O_7$ under similar conditions [24], i.e. 0.12 mol Li/mol 124 and 0.03 mol Li/mol 123 respectively, supporting again that Li ions are located in the 124 phase.

Acknowledgments

References

[1]   Wittingham M S and Jacobson A J 1982 *Intercalation Chemistry (Materials Science Series)* (New York: Academic)

[2] Murphy D W and Christian P A 1979 *Science* **205** 651
[3] Cava R J, Santoro A, Murphy D W, Zahurak S and Roth R S 1982 *J. Solid State Chem.* **42** 251
[4] Reilly J J, Suenaga M, Johnson J R, Thompson P and Moodenbaugh A R 1987 *Phys. Rev. B* **36** 5694
[5] Alario-Franco M A, Morán E, Várez A, Santamaría J and Sánchez-Quesada F 1990 *Solid State Ion.* **44** 73
[6] Várez A, Morán E, Alario-Franco M A, Santamaría J, González-Díaz G nd Sánchez-Quesada F 1990 *Solid State Commun.* **76** 917
[7] Señaris-Rodríguez M A, Várez A, Torrón C, Morán E and Alario-Franco M A 1992 *Physica and Materials Science of HTSC II (NATO ASI Series)* ed Kossowsky, Raveau and Patapis p 609
[8] Señariz-Rodríguez M A, Hetherington C J D, Várez A, Morán E and Alario-Franco M A 1991 *J. Solid State Chem.* **95** 388
[9] Zandbergen H W, Grownsky R, Wang K and Thomas G 1988 *Nature* **331** 596
[10] Marsh P, Fleming R M, Mandlich M L, de Santoro A M, Kwo J, Hong M and Martínez-Miranda L J 1988 *Nature* **334** 141
[11] Señaris-Rodríguez M A, Chippindale A M, Várez A, Morán E and Alario-Franco M A 1991 *Physica* C **172** 477
[12] Ngai K L, Mundy J L and Jain H 1989 *Phys. Rev. B* **39** 6169 and references therein
[13] Ngai K L 1993 *Phys. Rev. B* **48** 13481
[14] Meyer M, Maas P and Bunde A 1993 *Phys. Rev. Lett.* **71** 573
[15] Várez A 1993 *Doctoral Thesis* Universidad Complutense, Madrid
[16] Várez A, García Alvarado F, Morán E, Pingarrón J M and Alario-Franco M A *Physica* C at press
[17] Karpinski J, Kaldis E, Jilek E, Rusiecki S and Bucher B 1988 *Nature* **336** 660
[18] Jonscher A K 1983 *Dielectric Relaxation in Solids* (London: Chelsea Dielectric)
[19] Ngai K L 1979 *Comment. Solid State Phys.* **9** 127; 1980 *Comment. Solid State Phys.* **9** 141
[20] Kohlrausch R 1847 *Ann. Phys., Lpz* **72** 393
[21] Funke K 1993 *Prog. Solid State Chem.* **22** 111
[22] Dissado L A and Hill R M 1984 *J. Chem. Soc. Faraday Trans.* **80** 291
[23] Amador U, Várez A, Morán E and Alario-Franco M A 1993 *Solid State Ion.* **63–65** 518
[24] Señaris-Rodríguez M A 1992 *Doctoral Thesis* Universidad Complutense, Madrid